



Universidad Autónoma
de Madrid

Biblos-e Archivo
Repositorio Institucional UAM

Repositorio Institucional de la Universidad Autónoma de Madrid

<https://repositorio.uam.es>

Esta es la **versión de autor** del artículo publicado en:
This is an **author produced version** of a paper published in:

Physical Review A 105.3 (2022): 033104

DOI: <https://doi.org/10.1103/PhysRevA.105.033104>

Copyright: © 2022 American Physical Society

El acceso a la versión del editor puede requerir la suscripción del recurso
Access to the published version may require subscription

Asymmetric electron angular distributions in H_2 induced by intense ultrashort soft-X-ray laser pulses

Arturo Sopena,^{1,2} Fabrice Catoire,^{2,*} Alicia Palacios,^{1,3} Fernando Martín,^{1,4,5,†} and Henri Bachau^{2,‡}

¹*Departamento de Química, Módulo 13, Universidad Autónoma de Madrid, 28049 Madrid, Spain*

²*Centre des Lasers Intenses et Applications, Université de Bordeaux-CNRS-CEA, 33405 Talence Cedex, France*

³*Institute for Advanced Research in Chemical Sciences (IAdChem),*

Universidad Autónoma de Madrid, 28049 Madrid, Spain

⁴*Instituto Madrileño de Estudios Avanzados en Nanociencia (IMDEA-Nanociencia), Cantoblanco, 28049 Madrid, Spain*

⁵*Condensed Matter Physics Center (IFIMAC), Universidad Autónoma de Madrid, 28049 Madrid, Spain*

(Dated: January 25, 2022)

X-ray free-electron laser facilities generate nowadays ultrashort pulses with intensities as high as 10^{20} W/cm². The interaction of these light sources with atoms and molecules thus opens the way to still unexplored phenomena, where the commonly employed dipole approximation breaks down, and nonlinear excitation and ionization, as e.g. Raman and Compton-like processes, come into play. We have developed new theoretical tools to describe the interaction of intense attosecond soft-X-ray pulses with the hydrogen molecule in the photon energy ranging from 0.5 to 1.6 keV. We solve the time-dependent Schrödinger equation including both dipole and nondipole terms to obtain single ionization photoelectron spectra differential in both energy and angle of the ejected electron. The signature of stimulated Compton scattering is clearly seen in the photoelectron spectra just above the ionization threshold, where nondipole effects manifest. Remarkably, the interference between dipole- and nondipole-induced quantum paths leads to a significant asymmetry of the photoelectron angular distributions. We show that this asymmetry strongly depends on the relative direction of the light polarization and propagation vectors with respect to the molecular orientation.

I. INTRODUCTION

The last two decades have seen the advent of X-ray free-electron lasers (XFELs) throughout the world[1–8]. These facilities provide ultrashort pulses with unprecedented intensities (10^{20} W/cm²), over a large range of photon energies going from VUV to hard X-rays. XFELs can now routinely produce ultra-brilliant few-femtosecond (fs) pulses, allowing for an increasing number of applications in atomic and molecular physics, chemistry, material science, and biology [9–11]. Besides the impressive achievements in terms of brilliance, recent efforts are focusing on the generation and control of XFEL pulses with sub-fs (i.e., attosecond) durations [12]. For instance, single-spike XFEL pulses with pulse durations as short as 200 attoseconds have already been produced for photon energies in the range 4–10 keV [13]. We notice that the field of attoscience has been mainly driven by high-order harmonic generation (HHG) sources [14], which nowadays can produce pulses with durations as short as 43 attoseconds and have recently reached the soft X-ray spectral range [15–17]. However, production of X-ray pulses from HHG is still very challenging due to the low conversion efficiency of the HHG process in this energy range.

Extending the capabilities of XFELs to the attosecond domain is of crucial importance to perform real-time observations of electronic rearrangements in atoms

after core excitation or ionization [13, 18, 19]. Two-color time-resolved X-ray spectroscopy has been proposed to explore charge migration phenomena [20] or, as demonstrated in recent experiments, to retrieve images of the Auger-Meitner decay [21] in molecules with sub-femtosecond resolution. In addition, the high intensities of ultrashort XFEL pulses offer new perspectives [22–25] to study a manifold of nonlinear processes as, e.g., direct two-photon ionization in Ne^{8+} [26] or nonlinear Compton scattering in solid Be [27].

Soft X-ray pulses generated in synchrotrons have been recently employed in combination with multicoincident detection techniques, namely COLTRIMS [28], to retrieve for the first time fully differential Compton scattering (CS) cross sections in helium [29] and to measure photoemission time delays in H_2 with zeptosecond resolution [30]. The use of ultrashort XFEL pulses can bring new scenarios for Compton scattering due to their large bandwidth, as shown by recent theoretical work on stimulated Raman scattering from atoms [31, 32]. In this process, an X-ray photon is absorbed and another less energetic X-ray photon is emitted through a stimulated process in which the energy difference between the two photons is taken by a bound electron, which ends to an excited state. Stimulated emission is possible whenever photons with the energy of the emitted one are contained in the incoming light. When the energy difference between the two photons exceeds the ionization potential of the system, the process is similar to CS except that the second step is not a spontaneous process but a stimulated one and therefore is expected to lead to a strong contribution as compared to the unstimulated counter part. Hence this process is called *stimulated* Compton scatter-

* fabrice.catoire@u-bordeaux.fr

† fernando.martin@uam.es

‡ hbachau@orange.fr

ing (SCS) [33]. Owing to the close connection between the two processes, the CS cross sections can be easily obtained from the SCS ionization rate (see Eq. (15) in [34]). SCS can be a very efficient process when ultrashort pulses are used because their large bandwidth provides a wide range of photon energies to allow for X-ray stimulated emission and the ejection of low energy electrons, for which the CS cross section is maximum [35]. Furthermore, the high intensity and repetition rate of XFEL make them an ideal tool for multicoincidence detection, which is essential to determine the molecular orientation with respect to the light polarization direction in a photoionization event [30].

In this article, we present a novel scheme of SCS from the H_2 molecule using an intense ultrashort X-ray pulse. This work follows a recent communication [36] where SCS from H_2 was investigated in the few-hundred eV (~ 0.5 keV) energy range. In the present work, we extend the previous study with a thorough investigation of this process for photon energies ranging from 0.5 to 1.6 keV, with a focus on the dipole and nondipole contributions in photoelectron energy and angular distributions. We also describe in detail the theoretical methods that are required to include such a non-linear process, with emphasis on the necessary extensions in comparison with the usual dipole approximation. The short wavelength of the X-ray pulse breaks down the commonly employed dipole approximation and, as a consequence, the coherent contributions of dipole and nondipole terms lead to pronounced asymmetries in the photoelectron emission, which strongly depend on the X-ray wavelength and on the molecular orientation. This is a pure nonlinear effect that is better captured in the low-energy region of the photoelectron spectrum. The methodological and numerical details are given in section II. In section III, we present our results for the energy and angle differential ionization probabilities for different orientations of the light polarization and propagation vectors with respect to the molecular axis. Our results show strong variations of these distributions with the relative orientation of the light vector with respect to the molecular axis, as well as the effect of having two emitting centers. The main conclusions are summarized in section IV.

II. METHODOLOGY

The methodology used to describe the electronic structure of the isolated molecule and to solve the time-dependent Schrödinger equation (TDSE) has been described in detail in previous publications [37–40]. In the present work, the method has been extended to incorporate the explicit evaluation of nondipole corrections. In brief, the time-dependent wave function that represents the dynamics induced in the hydrogen molecule by an intense X-ray pulse (see section II A) is expanded in the basis of two-electron states built from antisymmetrized products of one-electron molecular orbitals, as explained

in sections II B and II C. This representation allows us to greatly reduce the computational effort and has proven to provide a very accurate representation of a manifold previously investigated light-induced processes in H_2 [39]. In this study, we mainly focus on disentangling the light parameters and molecular orientation dependencies of the relative contribution of dipole and the newly incorporated nondipole terms in the energy and angularly resolved electron emission. Due to the short duration of the X-ray pulses considered in our study, we will work within the fixed nuclei approximation. Atomic units (a.u.) are used throughout this paper unless otherwise stated.

A. Description of the laser- H_2 interaction

The nonrelativistic Hamiltonian representing the interaction of the H_2 molecule with a classical electromagnetic field is written, in the Coulomb gauge, as

$$\mathcal{H}(t) = \mathcal{H}_{el}(\mathbf{r}_1, \mathbf{r}_2) + \sum_{i=1,2} \mathbf{A}(\mathbf{r}_i, t) \cdot \mathbf{P}_i + \frac{1}{2} \sum_{i=1,2} \mathbf{A}(\mathbf{r}_i, t)^2, \quad (1)$$

where \mathcal{H}_{el} is the two-electron Hamiltonian of the isolated molecule, \mathbf{P}_i is the momentum operator for the electron i , and $\mathbf{A}(\mathbf{r}_i, t) = A(t - \boldsymbol{\eta} \cdot \mathbf{r}_i/c) \boldsymbol{\varepsilon}$ is the vector potential, where $\boldsymbol{\varepsilon}$ and $\boldsymbol{\eta}$ are the unitary vectors associated with the polarization, that is linear in this work, and the propagation direction of the field, respectively. \mathcal{H}_{el} is given by

$$\mathcal{H}_{el}(\mathbf{r}_1, \mathbf{r}_2) = -\frac{1}{2} \sum_{i=1,2} \nabla_i^2 - \sum_{i=1,2} \left[\frac{1}{|\frac{\mathbf{R}}{2} - \mathbf{r}_i|} + \frac{1}{|\frac{\mathbf{R}}{2} + \mathbf{r}_i|} \right] + \frac{1}{|\mathbf{r}_1 - \mathbf{r}_2|} + \frac{1}{R}, \quad (2)$$

where the vectors \mathbf{r}_1 and \mathbf{r}_2 refer to the positions of electrons 1 and 2, respectively, in the center of mass, \mathbf{R} is the internuclear separation vector, and R is the internuclear distance.

We approximate $A(t - \boldsymbol{\eta} \cdot \mathbf{r}_i/c)$ in Eq. (1) by the two lowest order terms of the Taylor expansion in $\boldsymbol{\eta} \cdot \mathbf{r}_i/c$,

$$A(t - \boldsymbol{\eta} \cdot \mathbf{r}_i/c) \simeq A(t) + F(t) \boldsymbol{\eta} \cdot \mathbf{r}_i/c, \quad (3)$$

with $F(t) = -\dot{A}(t)$. Hence, by neglecting the $1/c^2$ contributions, the Hamiltonian (1) can be rewritten

$$\mathcal{H} = \mathcal{H}_{el}(\mathbf{r}_1, \mathbf{r}_2) + A(t) \sum_{i=1,2} \boldsymbol{\varepsilon} \cdot \mathbf{P}_i + A(t)F(t) \sum_{i=1,2} \boldsymbol{\eta} \cdot \mathbf{r}_i/c + A(t)^2/2. \quad (4)$$

The last term $A(t)^2/2$ can be removed by performing a gauge transformation and, therefore, will not be explicitly considered in the following. In the above equation the term $\sum_{i=1,2} \mathbf{A}(\mathbf{r}_i, t) \cdot \mathbf{P}_i$ (see Eq. 1) is treated in dipole approximation for reasons explained in section II D. The vector potential amplitude $A(t)$ is written as

$$A(t) = f(t)A_0 \cos(\omega_0 t), \quad (5)$$

where ω_0 is the central laser frequency, A_0 is the peak amplitude of the vector potential, corresponding to a peak electric field $E_0 = A_0\omega_0$, i.e., an intensity $I = c|E_0|^2/(8\pi)$ (with $E_0 = 1$ a.u., corresponding to an intensity of 3.51×10^{16} W/cm²), and $f(t)$ is the pulse envelope, which has been chosen to be Gaussian. In this work, we have fixed the intensity to 10^{18} W/cm².

We have used the approximate Hamiltonian (4) to solve the TDSE that describes the laser-H₂ interaction

$$i \frac{\partial}{\partial t} \Psi(t) = \mathcal{H}(t) \Psi(t), \quad (6)$$

by expanding the time-dependent wave function $\Psi(t)$ in the basis of H₂ eigenstates Ψ_n^Λ with eigenenergies E_n^Λ (see section II B), so that

$$\Psi(t) = \sum_{n,\Lambda} C_{n,\Lambda}(t) \Psi_n^\Lambda(\mathbf{r}_1, \mathbf{r}_2) \exp\{[-iE_n^\Lambda t]\}. \quad (7)$$

After injection of the above expansion into Eq. (6) and projection onto the $\Psi_n^\Lambda(\mathbf{r}_1, \mathbf{r}_2)$ states, one obtains a system of coupled differential equations that is integrated from $t = -T$ to $t = T$ using an explicit time-adaptative Runge-Kutta method, with initial condition (at $t = -T$) corresponding to H₂ in the ground state ($X^1\Sigma_g^+$). T is chosen large enough such that the vector potential amplitudes $A(-T)$ and $A(T)$ have vanished. The wave function $\Psi(T)$ contains all the information on the molecular system at the end of the interaction. Relevant observables like photoelectron spectra or electron angular distributions are extracted by projecting $\Psi(T)$ onto field-free states, i.e., from the expansion coefficients $C_{n,\Lambda}(T)$ associated with the eigenstates $\Psi_n^\Lambda(\mathbf{r}_1, \mathbf{r}_2)$ [39].

The procedure described above, performed in velocity gauge with a multipole expansion of the vector potential, has been shown to be very efficient from the numerical point of view. Note that, as in the case of the dipole approximation, a transformation can be performed between the velocity and length gauges preserving the gauge invariance for an arbitrary n th order expansion of the vector potential [41]. A review of gauge invariance theory beyond the dipole approximation is also provided in [42].

B. Two-electron states of the H₂ molecule

We will only consider states of singlet spin multiplicity ($S = 0$), since these are the only ones that can be

populated in the nonrelativistic limit. We have used a configuration interaction (CI) procedure to calculate the bound states of H₂ at the equilibrium internuclear distance. Each term in the CI expansion is built as a symmetrized product of H₂⁺ one-electron wave functions ψ_n^m

$$\psi_{n_1, n_2}^{\Lambda; m_1, m_2}(\mathbf{r}_1, \mathbf{r}_2) = \frac{1}{\sqrt{2}} \{ \psi_{n_1}^{m_1}(\mathbf{r}_1) \psi_{n_2}^{m_2}(\mathbf{r}_2) + \psi_{n_1}^{m_1}(\mathbf{r}_2) \psi_{n_2}^{m_2}(\mathbf{r}_1) \}, \quad (8)$$

where we have factored out the spin component, which is antisymmetric, thus ensuring the antisymmetry of the two-electron configuration. The spatial component of the two-electron states are thus given by

$$\Psi_n^\Lambda(\mathbf{r}_1, \mathbf{r}_2) = \sum_{\substack{m_1, m_2 \\ \Lambda = |m_1 + m_2|}} \sum_{n_1, n_2} C_{n, n_1, n_2}^{m_1, m_2} \psi_{n_1, n_2}^{\Lambda; m_1, m_2}(\mathbf{r}_1, \mathbf{r}_2). \quad (9)$$

The coefficients $C_{n, n_1, n_2}^{m_1, m_2}$ and the eigenenergies E_n^Λ are obtained from a standard diagonalization procedure.

Notice that the two-electron states are characterized by the quantum number Λ , which represents the absolute value of the z component of the total angular momentum $L_z = l_{1,z} + l_{2,z}$, $\Lambda = 0$ (Σ), $\Lambda = 1$ (Π), $\Lambda = 2$ (Δ), etc. and the inversion symmetry of the states: gerade (g) or ungerade (u). We also note that there exists an additional symmetry associated with the reflection invariance of the Hamiltonian with respect to any plane containing the internuclear axis. According to this property, the Σ states are labeled $\Sigma_{g,u}^+$ for which the wave function is left unchanged upon reflection, or $\Sigma_{g,u}^-$ if it changes sign in performing that operation. The ground state of H₂ is denoted $X^1\Sigma_g^+$. As explained in the following sections, the selection rules imposed by the operators describing the light-matter interaction require the evaluation of bound and continuum states of $^1\Sigma_{g,u}^+$, $^1\Pi_u$ and $^1\Delta_g$ molecular symmetries.

The evaluation of the two-electron single-continuum states requires special treatment, since a direct diagonalization on a two-electron basis does not lead to the correct asymptotic behavior. The procedure has been explained in [38], so here we only recall the main steps. First, we determine two-electron uncoupled-continuum states $\psi_E^{\nu\lambda lm}$ (UCS) associated with each partial wave l in each open ionization channel ν with symmetry λ (the z component of the angular momentum l_z and the inversion symmetry of the remaining electron). The scattering states with proper incoming boundary conditions are related to the UCS through the well known Lippmann-Schwinger equation:

$$\Psi_{\nu\lambda lm, E}^- = \psi_E^{\nu\lambda lm} + G^-(E) V \psi_E^{\nu\lambda lm}, \quad (10)$$

where $G^-(E)$ is the usual Green function $G^-(E) = (E + i\gamma - \mathcal{H}_{el})^{-1}$ with $\gamma \rightarrow 0^-$ and V is the interchannel coupling. Using the closure relation and the basis of

UCSs, Eq. (10) leads to a system of linear equations that is then solved for each energy E in the continuum.

For the calculation of the bound states, we include between 390 and 700 configurations built from H_2^+ orbitals, depending on the symmetry of the two-electron wave function. To improve the description of the ground state at the equilibrium distance $R_e \sim 1.4$ a.u., a supplementary basis set of Slater-type orbitals (STOs) is included in the CI expansion. These additional basis functions are of the form $r^n e^{-\gamma_{nl}r} \cdot Y_l^m(\theta, \phi)$, with $n = 1 - 10$, $l = 0 - 11$ and $\gamma_{nl} = 2.8$ for all n and l . Each UCS of H_2 is built from 280 configurations representing an electron in a given state of H_2^+ and a scattered electron with angular momentum l . This configuration basis allows us to properly describe continuum wave functions up to an electron energy of 80 a.u. Given the high electronic energies considered in this work, the multichannel character of the wave function has to be thoroughly examined, especially with regard to the number of ionization thresholds included. We found that, if one is interested in measurements of photoelectron spectra and photoelectron angular distributions that do not distinguish between dissociative and non-dissociative channels, only the first ionization threshold $1s\sigma_g$ and partial waves up to $l = 7$ need to be considered.

C. The one-electron states of H_2^+

The one-electron molecular orbitals of H_2^+ used to build the two-electron configurations are the solution of the Schrödinger equation

$$h_{el}\psi_n = E_n\psi_n, \quad (11)$$

where h_{el} is the nonrelativistic one-electron Hamiltonian of H_2^+ given by

$$h_{el}(\mathbf{r}) = -\frac{1}{2}\nabla^2 - \frac{1}{|\frac{\mathbf{R}}{2} - \mathbf{r}|} - \frac{1}{|\frac{\mathbf{R}}{2} + \mathbf{r}|} + \frac{1}{R}. \quad (12)$$

The vector \mathbf{r} refers to the electron position in the center of mass.

This equation is solved by expanding the electronic wave function ψ_n in a basis of radial B-splines multiplied by spherical harmonics. If the direction of the internuclear axis is taken along the z -axis, then ψ_n is also an eigenfunction of the operator l_z with eigenvalues $m = 0, \pm 1, \pm 2$, etc. The expansion reads

$$\psi_n^m(\mathbf{r}) = \sum_{l=0}^{l_{max}} \sum_{i=1}^{N_l} c_{il}^n \frac{B_i^k(r)}{r} Y_l^m(\theta, \phi), \quad (13)$$

where N_l is the number of B-spline functions $B_i^k(r)$. B-splines are piecewise polynomials of order k defined in a box of length r_{max} [37]. Substitution of expansion (13) into Eq. (11) and projection onto the $B_i^k(r)Y_l^m(\theta, \phi)$ basis leads to a generalized eigensystem problem. A diagonalization procedure is used to calculate the coefficients

c_{il}^n in Eq. (13), providing a set of eigenfunctions ψ_n^m and associated eigenenergies E_n^m . In the expansion (13), the inversion symmetry affects only the spherical harmonic $Y_l^m(\theta, \phi)$, so that only even (odd) values of the angular momentum contribute to orbitals of gerade (ungerade) symmetry.

For the one-center spherical expansion of the H_2^+ orbitals, we have used a set of 280 B-splines of order 8 and spherical harmonics up to $l = 16$. The B-spline functions are defined in an electronic radial box of length $|\mathbf{r}_{max}| = 60$ a.u. with $\psi_n^m(\mathbf{r}_{max}) = 0$ and the proper boundary conditions at the origin.

D. Transitions induced by the laser interaction

In order to rationalize the different coupling terms in Eq. (1), we recall the expression for stimulated Compton transition amplitudes in second-order of perturbation theory. We consider a transition between a bound state $|g\rangle$ and a final state $|f\rangle$ of energies E_g and E_f , respectively. We choose a field polarization along the z axis of the reference system ($\boldsymbol{\varepsilon} \cdot \mathbf{P}_i = P_{i,z}$), the generalization to other polarization directions is straightforward. The transition amplitude has the general form [32]

$$\mathcal{A}_{gf} \propto \int_{\omega_{fg}/2}^{\infty} d\omega \tilde{A}(\omega) \tilde{A}(\omega_{fg} - \omega) \mathcal{M}_{fg}^{\text{KHW}}(\omega, \omega - \omega_{fg}) \quad (14)$$

where $\tilde{A}(\omega)$ is the Fourier transform of the vector potential amplitude $A(t)$ and $\omega_{fg} = E_f - E_g$. $\mathcal{M}_{fg}^{\text{KHW}}(\omega, \omega - \omega_{fg})$ refers to the Kramers-Heisenberg-Waller (KHW) matrix element [43, 44] which defines the differential cross section for Compton scattering from a bound state [45]. It reads

$$\begin{aligned} \mathcal{M}_{fg}^{\text{KHW}}(\omega, \omega') = & \langle f | \sum_i e^{-i\mathbf{k}' \cdot \mathbf{r}_i} P_{i,z} G^{(+)}(E_g + \omega) \sum_i e^{i\mathbf{k} \cdot \mathbf{r}_i} P_{i,z} | g \rangle \\ & + \langle f | \sum_i e^{i\mathbf{k} \cdot \mathbf{r}_i} P_{i,z} G^{(+)}(E_g - \omega') \sum_i e^{-i\mathbf{k}' \cdot \mathbf{r}_i} P_{i,z} | g \rangle \\ & + \sum_i \langle f | e^{i(\mathbf{k} - \mathbf{k}') \cdot \mathbf{r}_i} | g \rangle. \end{aligned} \quad (15)$$

$G^+(E) = (E + i\gamma - \mathcal{H}_{el})^{-1}$ with $\gamma \rightarrow 0^+$ is the so-called Green function. The two frequencies ω and ω' are connected by $\omega - \omega' = \omega_{fg}$. \mathbf{k} and \mathbf{k}' are the photon wave vectors of the absorbed and emitted photons, respectively; $\mathbf{k} = \omega \boldsymbol{\eta}/c$ and $\mathbf{k}' = \omega' \boldsymbol{\eta}/c$. The first two terms represent the second-order contribution in perturbation theory (PT) of the coupling term $\mathbf{A} \cdot \mathbf{P}$, associated with the absorption of the photon ω and emission of ω' . In previous works reporting stimulated Compton and Raman scattering in atoms [32, 33], it has been shown that the nondipole correction associated with $\mathbf{A} \cdot \mathbf{P}$ plays a negligible role. Therefore, the second-order term in PT

associated with $\mathbf{A} \cdot \mathbf{P}$ can be treated in the dipole approximation. The third term in Eq. (15) refers to the nondipole contribution \mathbf{A}^2 . This term has been shown to play a crucial role in Compton and Raman scattering and is usually written

$$\left\langle f \ e^{i(\mathbf{k}-\mathbf{k}') \cdot \mathbf{r}} \ g \right\rangle = f \ e^{i\mathbf{Q} \cdot \mathbf{r}} \ g, \quad (16)$$

where

$$\mathbf{Q} = \mathbf{k} - \mathbf{k}' = (\omega - \omega')\boldsymbol{\eta}/c, \quad (17)$$

is the momentum transfer vector. As we will see below $\omega - \omega'$ is of the order of a few a.u., so that $(\omega - \omega')/c \ll 1$ and we can retain only the first two terms in the Taylor expansion of $e^{i\mathbf{Q} \cdot \mathbf{r}}$

$$e^{i\mathbf{Q} \cdot \mathbf{r}} \simeq 1 + i\mathbf{Q} \cdot \mathbf{r}. \quad (18)$$

It is worth noticing that both the ionization rate associated with \mathbf{A}^2 to first-order in the momentum transfer and the rate associated with $\mathbf{A} \cdot \mathbf{P}$ to second-order in PT vary quadratically with the field intensity.

From the above approximations, it is easy to extract the selection rules associated with $\mathbf{A} \cdot \mathbf{P}$ (in the dipole approximation) and \mathbf{A}^2 (up to $1/c$). We investigate all possible light-molecule configurations, with the polarization oriented along the z or x/y -axis, i.e., parallel or perpendicular to the internuclear axis, respectively. For the transitions of second-order in $\mathbf{A} \cdot \mathbf{P}$, the selection rules are the following (the polarization is indicated on the top of the arrows, each arrow representing a one-photon transition):

$$\begin{aligned} X^1\Sigma_g^+ &\xrightarrow{\epsilon_z} \Sigma_u^+ \xrightarrow{\epsilon_z} \Sigma_g^+ \\ X^1\Sigma_g^+ &\xrightarrow{\epsilon_x/\epsilon_y} \Pi_u \xrightarrow{\epsilon_x/\epsilon_y} \Sigma_g^+, \Delta_g. \end{aligned} \quad (19)$$

Considering now the transition associated with \mathbf{A}^2 we study the cases where the propagation direction $\boldsymbol{\eta}$ is along the z -axis or along x or y . Treated in first-order of perturbation theory and neglecting the corrections in $1/c^2$, the selection rules give (the propagation direction is indicated on the top of the arrow);

$$\begin{aligned} X^1\Sigma_g^+ &\xrightarrow{\eta_z} \Sigma_u^+ \\ X^1\Sigma_g^+ &\xrightarrow{\eta_x/\eta_y} \Pi_u \end{aligned} \quad (20)$$

We notice that the dipole transition leads to gerade (g) final states while the nondipole one populates ungerade (u) states.

III. RESULTS AND DISCUSSION

We assume that the hydrogen molecule is initially in its ground state and that it interacts with an ultrashort

X-ray pulse. The large energy bandwidth of the ultrashort pulse makes energetically accessible both stimulated Raman scattering (SRS) and stimulated Compton scattering (SCS), i.e., absorption and subsequent stimulated emission of photons, within a single pulse, leading to molecular excitation (SRS) and ionization close to threshold (SCS). For the present simulations, we have used a linearly polarized Gaussian-shaped pulse with a full-width half maximum (FWHM) in time of 66 attoseconds (i.e., an energy bandwidth of $\simeq 2$ a.u.) and a peak intensity of 10^{18} W/cm². We note that the SCS process occurs because the energy bandwidth is much larger than the ionization threshold (0.6 a.u.). For a pulse duration of about 200 attoseconds, corresponding to an energy bandwidth (FWHM) equal to the ionization potential, SCS is still possible but the magnitude of the resulting peak would be smaller. For longer pulse durations, SCS would not be observed since two photons ω_1 and ω_2 with an energy difference of at least 0.6 a.u. cannot be found within the pulse bandwidth with sufficient intensity. All calculations are performed solving the TDSE, as explained in section II A. We have computed angle and energy differential ionization yields for pulses with three different central frequencies: $\omega_0 = 20, 40$, and 60 a.u. (i.e., ≈ 544 eV, ≈ 1.1 keV, and ≈ 1.6 keV). As shown in the above introduced studies of SCS in atoms, the dipole approximation is expected to break down at these photon energies and, therefore, we have included both dipole and nondipole contributions through the Hamiltonian defined in Eq. (4). Due to the high photon energies, the Keldysh parameter γ [46], which marks the limit between the perturbative ($\gamma > 1$) and the nonperturbative ($\gamma < 1$) regime, is much larger than 1 and we therefore expect that the laser-molecule interaction process remains in the perturbative regime despite the high peak intensity values. In Fig. 1(a) we present a sketch of the SCS process in H₂, with the energy bandwidth of the pulse depicted as a purple shadow. In this single-pulse scheme, the photoabsorption and the stimulated emission processes lead to molecular ionization with an absorbed effective energy equal to the energy difference between two photons of energy within the bandwidth of the pulse: a more energetic photon that is absorbed and a slightly less energetic photon that is emitted. It should be noted that the same process can be induced by employing a scheme using longer pulse durations but combining two pulses with different colors [33]. Our scheme, employing a single attosecond pulse, has been chosen to show the main features arising in molecular SCS using H₂ as a benchmark, but keeping the computational effort within reasonable boundaries.

A. Photoelectron spectra

The photoelectron spectrum resulting from the interaction of the hydrogen molecule with an X-ray pulse with the characteristics mentioned above and a central fre-

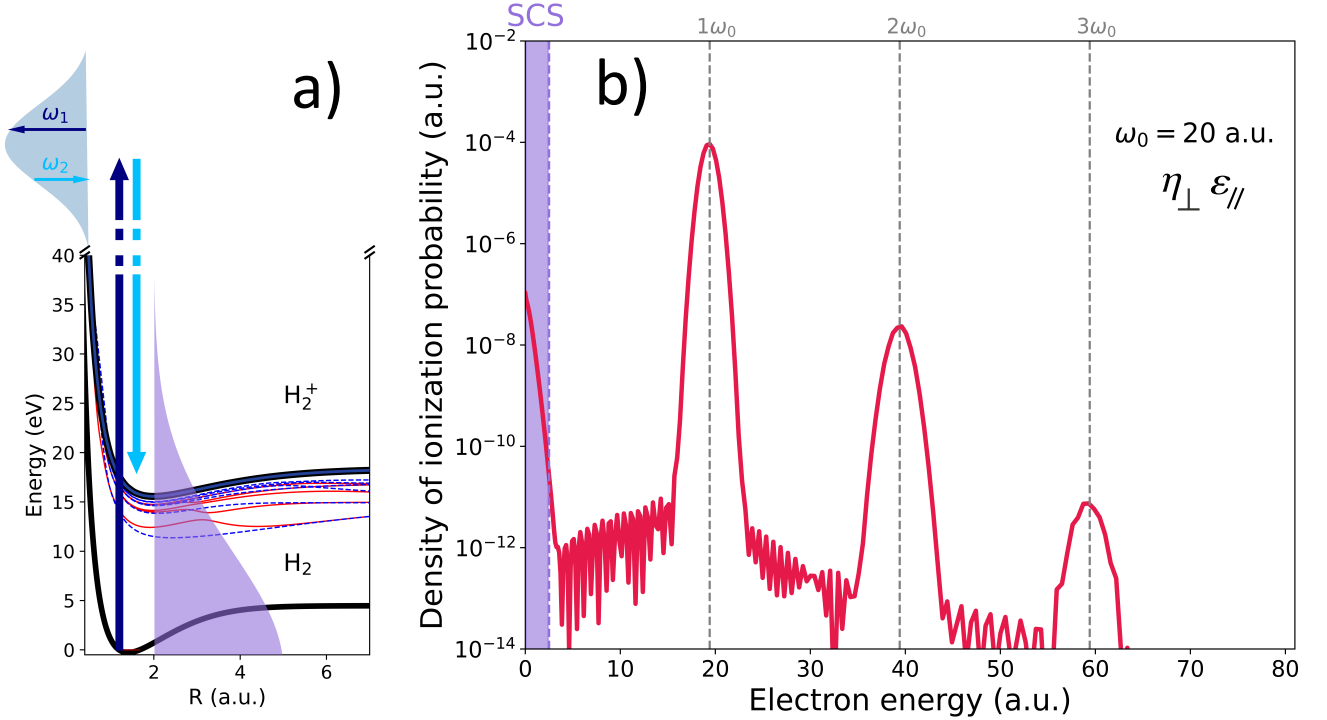


FIG. 1. (a) Schematic representation of the SCS process leading to the ejection of low-energy electrons. The thin dashed blue line and thin red line represent the lowest excited states of H_2 of $1^1\Sigma_u^+$ and $1^1\Sigma_g^+$ symmetries, respectively. The two thick lines represent the ground state of H_2 (lower line) and H_2^+ (upper line). The energy bandwidth of the pulse is depicted by a blue shadow in the region of one-photon absorption (left top of the figure, not at scale), and by a purple shadow in the region of stimulated Raman and Compton scattering. Note that the shape of the energy bandwidths (magnitude of the energy bandwidth along the x -direction provided in abscissa on the figure) has been arbitrarily fixed for the sake of clarity. (b) Photoelectron spectrum for a 66 attoseconds pulse centered at $\omega_0 = 20$ a.u. (544 eV) for parallel polarization ($\epsilon_{//}$) and perpendicular (η_{\perp}) propagation of the light with respect to the molecular axis. The purple shadowed area indicates the energy region where SCS manifests itself (electron energies 0-2.5 a.u.). Vertical dashed lines indicate the position of the ATI absorption peaks, stemming from the absorption of 1, 2, and 3 photons.

quency $\omega_0 = 20$ a.u. (544 eV) is shown in Fig. 1(b). The light polarization vector is placed along the molecular axis and, therefore, the propagation direction is perpendicular to it, as illustrated in panel A of Fig. 2. The spectrum presents three large peaks associated with the absorption of one, two, and three photons from the H_2 ground state (indicated by vertical dashed lines in the figure), appearing at 19.4, 39.4, and 59.4 a.u. photoelectron energies. The ionization potential of H_2 at the equilibrium distance $R_e = 1.4$ a.u. is close to 0.6 a.u. These three strong peaks leading to single-photon ionization (ω_0) and above-threshold ionization (ATI) ($2\omega_0$ and $3\omega_0$), are perfectly reproduced within the dipole approximation. Note that the oscillations observed in Fig. 1(b) appearing in between consecutive ATI peaks where the signal is very low, are not physical but originate from the limited accuracy of the numerical approach. However, we also find a significant contribution close to the ionization threshold, at electron energies 0-2.5 a.u., which results from the absorption of a photon and the stimulated

emission of another one, and therefore corresponds to the SCS process. We have checked that the ionization rate in this region varies quadratically with the peak intensity, which confirms that, at these low photoelectron energies, the process is driven by two-photon transitions. We note that the choice of an intensity of 10^{18} W/cm² has been made so that the SCS ionization signal is large enough to overcome the typical noise level of multicoincidence experiments. Asymmetries similar to those described in this work would be found at lower intensities, but due to the I^2 scaling, they would be much harder to detect due to the lower ionization probability. As explained above, the laser bandwidth ($\simeq 2$ a.u.) is larger than the ionization potential, energetically enabling electron emission over an energy range of the order of 1 a.u. above threshold. Although not shown here, similar photoelectron spectra are found for pulses centered at 40 and 60 a.u., i.e. every spectrum contains the one-photon and the ATI peaks as well as the increased yield due to SCS appearing close to threshold. However, while for the one-photon and ATI

peaks the dipole contribution (see Eq. 4) totally dominates, irrespective of the central energy of the pulse and of the molecular orientation, the SCS signal is modulated by both dipole and nondipole terms, whose relative contribution is strongly dependent on laser parameters and molecular orientation.

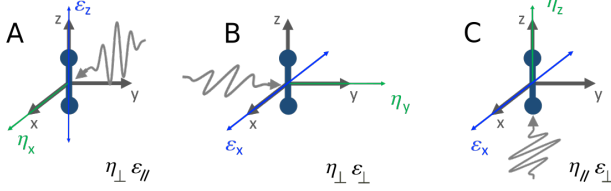


FIG. 2. The three configurations investigated in this article showing of the light polarization (ϵ) and propagation (η) vectors with respect to the molecular axis (along the z -axis).

In Fig. 2, we show three typical light-molecule configurations for a diatomic homonuclear molecule. Obviously, for atomic systems, the spherical symmetry makes these three scenarios equivalent. It should be noticed however that for the molecular case, assuming now the H_2 molecule along the z -axis, there is a second equivalent configuration in each case by exchanging the x and y -axis. For instance, in the A configuration, the nondipole (A^2) rates are equal if the propagation proceeds along x or y , and only a rotation of $\pi/2$ of the azimuthal angle in the angular distributions would be expected for this term. For the same reasons, the dipole-induced signal is the same for B and C, and placing the polarization vector in the y -axis for C, again, would only yield a $\pi/2$ rotation in the angular distributions. As a consequence, as we discuss next, one can achieve a different degree of control by manipulating the laser parameters for different molecular orientations.

We analyze the SCS signal, i.e., the electron energy region ranging from 0 to 2.5 a.u. (purple shadowed area in Fig. 1(b)) for the three possible configurations A, B, and C depicted in Fig. 2. The calculated photoelectron spectra for three pulses with different central frequencies ($\omega_0 = 20, 40$, and 60 a.u.) are shown in Fig. 3. In addition to the total ionization yields, the figure shows the contributions from final states of different symmetries accessible by the two-photon SCS process.

We first focus on the A configuration in Fig. 2: light polarization vector (ϵ_{\parallel}) parallel to the molecular axis, which is thus perpendicular to the light propagation direction (η_{\perp}), in this case along the x -axis (η_x). In a two-photon process, the dipole operator will then couple the ground state of H_2 , $X^1\Sigma_g^+$, with electronic continuum states of $1\Sigma_g^+$ symmetry, while the nondipole correction A^2 (calculated to first-order in $1/c$) will populate states of $1\Pi_u$ symmetry (see selection rules in Eqs. (19) and

(20)).

The left column in Fig. 3 shows the ionization probability densities for the three pulses ($\omega_0 = 20, 40$, and 60 a.u.) for the A configuration ($\eta_{\perp}\epsilon_{\parallel}$). We plot the contribution of dipole ($A \cdot P$ in full green and purple lines for symmetries $1\Sigma_g^+$ and $1\Delta_g$, respectively) and nondipole (A^2 in dashed lines, in red color for $1\Sigma_u^+$ and orange for $1\Pi_u$) coupling terms, as well as the total density of probability (thick full blue line). For the three pulses, the nondipole contribution ($1\Pi_u$) dominates over the dipole one ($1\Sigma_g$) in the whole photoelectron energy range where SCS manifests, this trend being more pronounced as ω_0 increases. For the 20 a.u. pulse, the nondipole contribution is approximately one order of magnitude larger than the dipole counterpart for absorbed energies very close to threshold, but these contributions come closer as the photoelectron energy reaches 2.5 a.u. For 40 and 60 a.u. central frequencies, however, the nondipole contribution is two and three orders of magnitude larger, respectively, and it remains as the dominant term over the whole energy range up to 2.5 a.u. In fact, from Eq. (15), one can show that the dipole and nondipole probabilities scale as $1/\omega_0^8$ and $1/\omega_0^4$, respectively, for a given intensity. This propensity rule works very well for the three configurations shown in Fig. 3.

The unexpectedly low contribution of the dipole term in SCS has been already explained in previous studies [47] and can be understood as the result of the partial cancellation of the second-order dipole terms in Eq. (15) [33]. This partial cancellation of dipole amplitudes occurs for every molecular symmetry involved in the second-order dipole terms, and therefore, results in a decrease of this term for any orientation of the light with respect to the molecule. However, as shown below, the relative strength of both dipole and nondipole contributions depends on the orientation of the molecular axis with respect to the polarization and propagation directions, so that one finds a quite distinct behavior for each orientation.

For the B configuration, illustrated in Fig. 2 B, the light polarization vector is now perpendicular to the molecular axis (ϵ_{\perp} along the x -axis), while the propagation direction is still perpendicular to it (η_{\perp} along the y -axis). The coupling terms associated with nondipole corrections (A^2) are thus the same as in the previous configuration, leading to a population of final states of $1\Pi_u$ symmetry. Therefore, the ionization probability densities associated with $1\Pi_u$ final states in Fig. 3 panels b, e and h are the same as those resulting from the A configuration, Fig. 3 panels a, d and g. However, the dipole selection rules for a two-photon process now allow for transitions to $1\Sigma_g^+$ and $1\Delta_g$ final state symmetries, undergoing a second-order process through intermediate $1\Pi_u$ states (see Eq. 19). As has been shown in previous works on H_2 [39, 48], dipole couplings connecting the ground and the excited states of H_2 are significantly larger when the molecule is perpendicular to the polarization vector. Consequently, the dipole contribution in the B configuration is larger than that in the parallel case

(A configuration). As a result, for a 20 a.u. pulse in the B configuration ($\eta_{\perp}\varepsilon_{\perp}$) (Fig. 3 panel b), the SCS signal is now dominated by the dipole terms over the whole range of photoelectron energies. However, according to the scaling laws mentioned above, the dipole contributions scale as $1/\omega_0^8$ while the nondipole ones scale as $1/\omega_0^4$, so that dipole-induced transitions become less important for the larger central frequencies. We thus find that, for 40 and 60 a.u. pulses (Fig. 3 panels e and h), the nondipole corrections are still the dominant contributions to the SCS signal.

For the C configuration, depicted in Fig. 2 C, the light polarization vector is kept perpendicular to the molecular axis (ε_{\perp} along the x -axis as in the B configuration), but with the propagation direction parallel to it ($\eta_{//}$). As for the dipole terms, the nondipole correction terms (\mathbf{A}^2) become smaller when the direction of the corresponding operator is parallel to the molecular axis. Consequently, while the dipole contribution remains as in the B configuration, the nondipole correction will decrease significantly with respect to the previous case. In the C configuration, for the 20 a.u. pulse (Fig. 3 panel c), the dipole contribution is the dominant channel in the whole energy range. For the 40 a.u. pulse (Fig. 3 panel f), the nondipole corrections are still dominant up to photoelectron energies of 1.0 a.u., and they are overcome by the dipole contributions as the electron energy becomes larger. Even for the 60 a.u. pulse, where the nondipole terms are more than an order of magnitude larger close to threshold, the dipole contribution becomes quickly dominant, overtaking for photoelectron energies above 1.5 a.u.

In a nutshell, Fig. 3 represents a quick summary of the interplay between the underlying mechanisms responsible for SCS and their relative importance as a function of energy and molecular orientation. In brief, the larger the central frequency of the pulse and the smaller the photoelectron energy, the more probable is to observe nondipole-induced SCS. More interestingly, the nondipole SCS becomes dominant over the dipole-induced counterpart when the molecular axis is perpendicular to the light propagation direction, being even more favorable when the light polarization direction is kept parallel to the molecular axis.

Notice that for every light-molecule configuration and every pulse investigated here, the dipole terms become quickly dominant for electron energies larger than 2.5 a.u., so that the largest ionization probability corresponds to the one-photon absorption process (first-order dipole) at $E_e = \omega_0 - \text{IP}$, leading to the peak at $1\omega_0$ in Fig. 1(b). As expected, the SCS probability is of the order of the second-order dipole transition at around $E_e = 2\omega_0 - \text{IP}$ (first ATI peak, at $2\omega_0$ as shown in Fig. 1(b)), a feature also observed in atoms. However, the two-center character of the molecule provides a novel aspect in SCS and ATI: the fact that the total angular momentum is not conserved and, consequently, the ejected electron is described by a coherent superposition of spherical harmonics with the same m but different l .

Therefore, in the molecular case, the relative contribution of the second-order dipole terms does not follow the patterns found in atoms, which in the case of an initial state with $l = 0$ predicts population of $l=0$ (S) and $l = 2$ (D) states. The calculations show that stimulated Raman and Compton processes in the hydrogen atom favor the $l=0$ channel over the $l=2$ one [32, 35]. Instead, for example in the case of perpendicular polarization, we have found a larger probability for $^1\Sigma_g^+$ with $l = 4$.

B. Molecular frame photoelectron angular distributions

From the experimental point of view, it is not possible to retrieve from the photoelectron spectra the different contributions of dipole and nondipole-induced SCS probabilities, nor the relative weight associated with each final symmetry or partial waves. However, the interplay between these paths can be experimentally captured when measuring the angular distributions of the emitted electrons. These are very sensitive to small variations in the relative contributions from distinct quantum paths. The dominant final symmetry will lead to an electron emission favoring some specific directions, and the detailed information on the dominant terms can be experimentally retrieved to a large extent from the molecular frame photoelectron angular distributions (MFPADs).

The MFPADs shown in Fig. 4 have been obtained solving the TDSE with the full Hamiltonian (see Eq. 4), after integrating over electron energies in the range $[0 - 2.5]$ a.u. (purple shadowed region in Fig. 1(b), equivalently, whole energy range shown in every panel in Fig. 3). For the sake of clarity, we follow the same layout as in Fig. 3. Each column corresponds to a given light configuration with respect to the molecular axis, configurations A ($\eta_{\perp}\varepsilon_{//}$), B ($\eta_{\perp}\varepsilon_{\perp}$), and C ($\eta_{//}\varepsilon_{\perp}$) as depicted in Fig. 2. Each row corresponds to the results for a given pulse, centered at $\omega_0 = 20, 40$, and 60 a.u.

One can see that every MFPAD, for the three limiting cases, presents a symmetry plane for the electron emission defined by the light, i.e., the plane containing the polarization and propagation vectors.

When nondipole-induced SCS dominates, e.g. at 60 a.u. in the A configuration (bottom row, left panel in Fig. 4), the electrons are emitted following a cosine-squared-like distribution with respect to the light propagation direction (η_x), and with a cylindrical symmetry around this axis, compatible with a final $^1\Pi_u$ symmetry of the system. The H_2^+ ion is left in its ground state, $1s\sigma_g$, and electrons are emitted with odd angular momenta, $l = 1$ being the dominant partial wave. As the photon energy decreases, the dipole contribution increases (see Fig. 3), and the interference between the different quantum paths distorts the distribution, which becomes asymmetric along the propagation direction, i.e. with respect to the plane containing the polarization vector and perpendicular to the propagation direction.

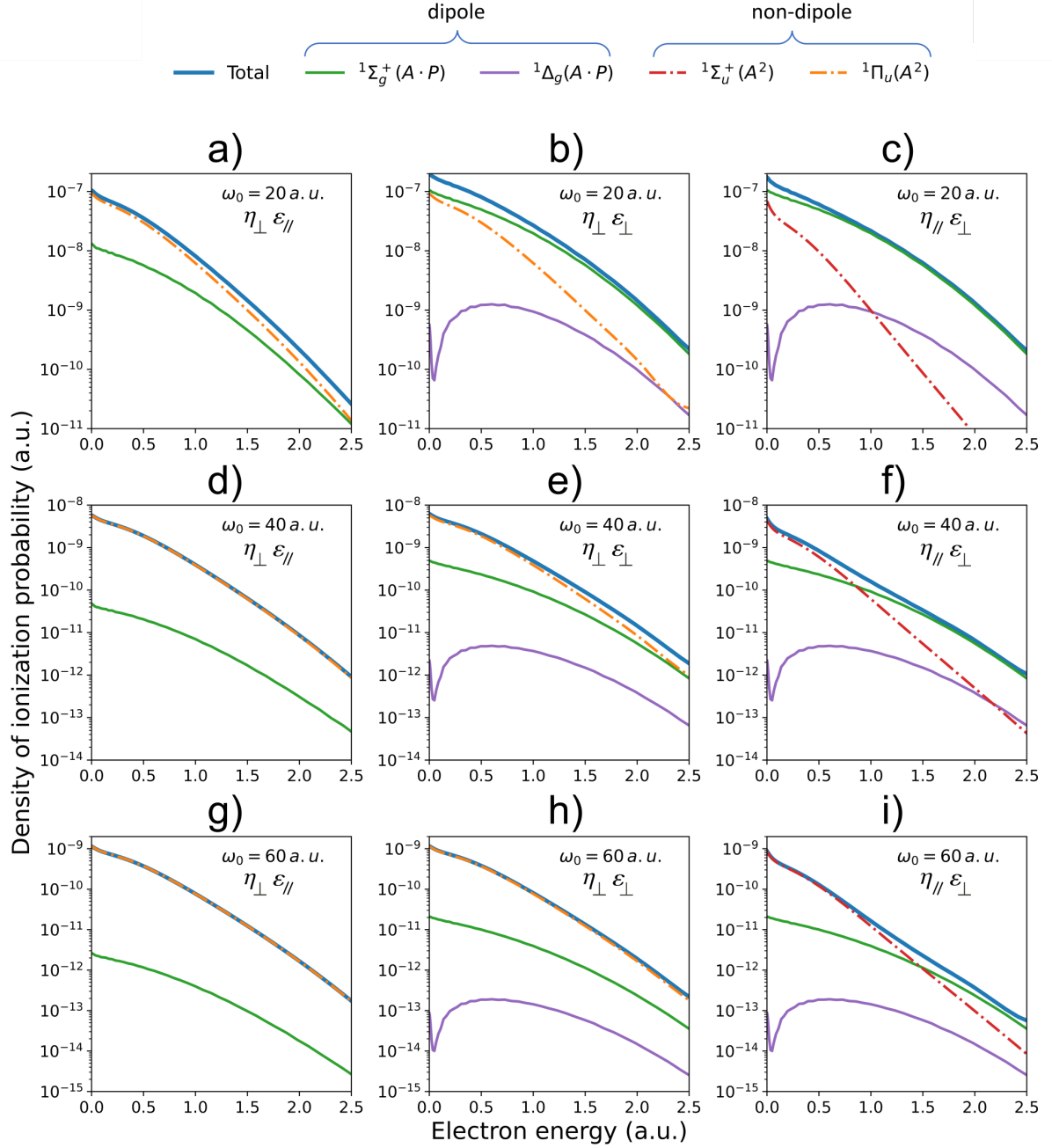


FIG. 3. Photoelectron spectra for three different pulses, centered at $\omega_0 = 20$ a.u. (a,b,c), $\omega_0 = 40$ a.u. (d,e,f), and $\omega_0 = 60$ a.u. (g,h,i). Each column corresponds to a given configuration for the light polarization and propagation directions with respect to the molecular axis as plotted in Fig. 2. Thick blue lines are the total ionization yields. Green and purple full lines are the contributions from the dipole terms. Red and orange dashed-dotted lines are the contributions from the nondipole terms.

This symmetry breaking in the photoelectron emission results from the coherent contribution of dipole-induced transitions populating $^1\Sigma_g^+$ states and nondipole-induced transitions reaching the $^1\Pi_u$ symmetry. This effect becomes more apparent for the lower photon energies as

shown in the left column in Fig. 4. The same trend is found in the middle column of Fig. 4, for the B configuration ($\eta_\perp \varepsilon_\perp$). Again, since the SCS signal is dominated by the nondipole term (\mathbf{A}^2), the electron emission for the largest photon energies mostly follows the propagation direction, η_y , with a cylindrical symmetry around it. A

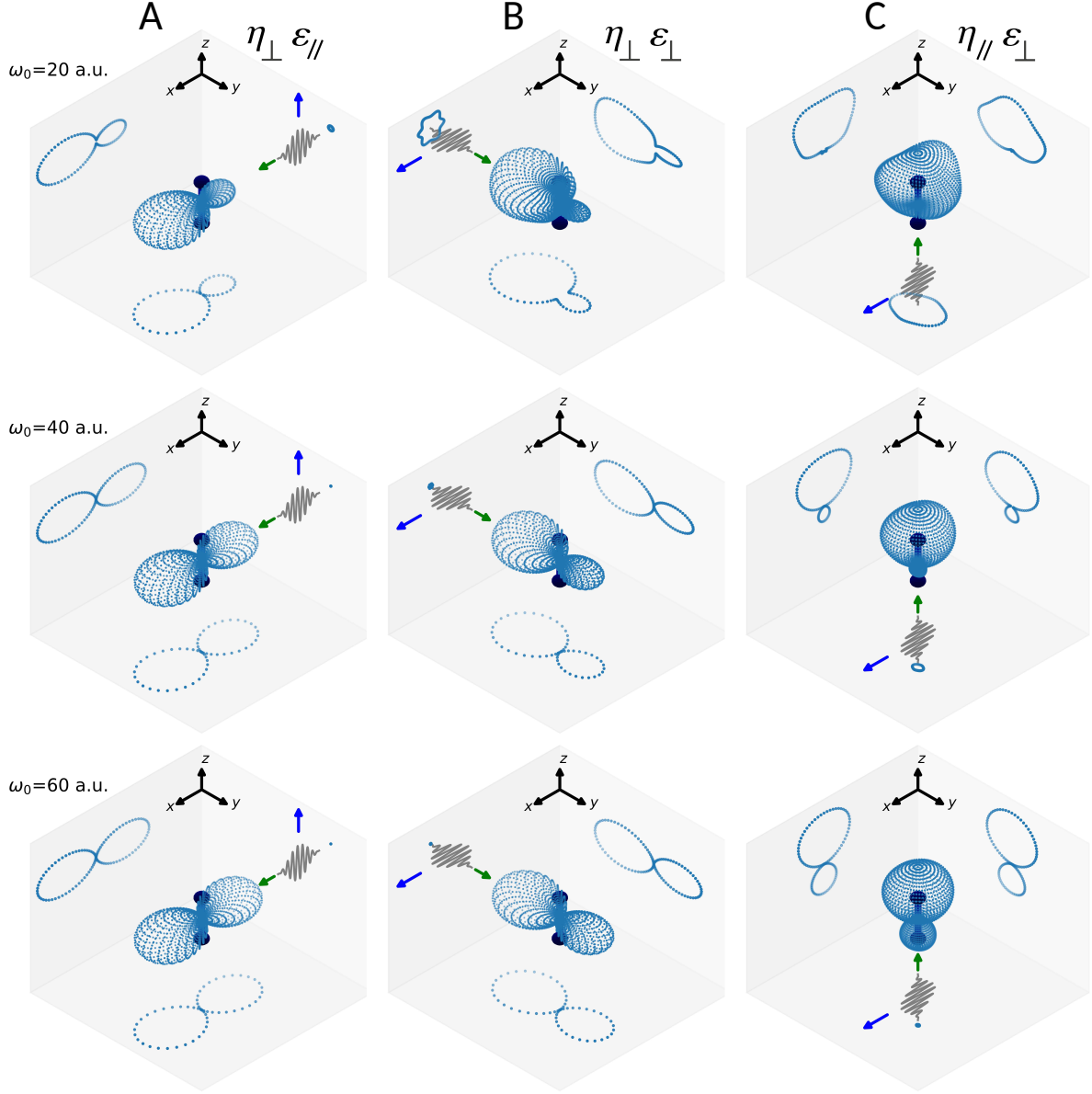


FIG. 4. Molecular frame photoelectron angular distribution (MFPAD) integrated over electron energies over the range $[0 - 2.5]$ a.u. (purple shadowed region in Fig. 1(b), or equivalently the whole energy range shown in every panel in Fig. 3). Each row corresponds to the results for a given pulse, centered at $\omega_0 = 20, 40$, and 60 a.u. Each column corresponds to a given light configuration with respect to the molecular axis, configurations A, B, and C as depicted in Fig. 2.

more pronounced asymmetry is now found in the electron emission for $\omega_0 = 20$ a.u., because (see Fig. 3) dipole and nondipole terms coherently contribute significantly to the electron emission at different angles, while at 60 a.u. it is mostly the nondipole terms that are predominant. Note that the angular distributions for 60 a.u. in the A and B configurations are rather similar, following the propaga-

tion direction η . This is explained by the fact that the nondipole contribution into the $^1\Pi_u$ states is the dominant one and it is indistinguishable in the photoelectron spectra as shown in Fig. 3. It can be only distinguished because the propagation direction is placed in the x -axis for the A configuration, while for the B configuration it follows the y -axis. Interestingly, for the B configuration,

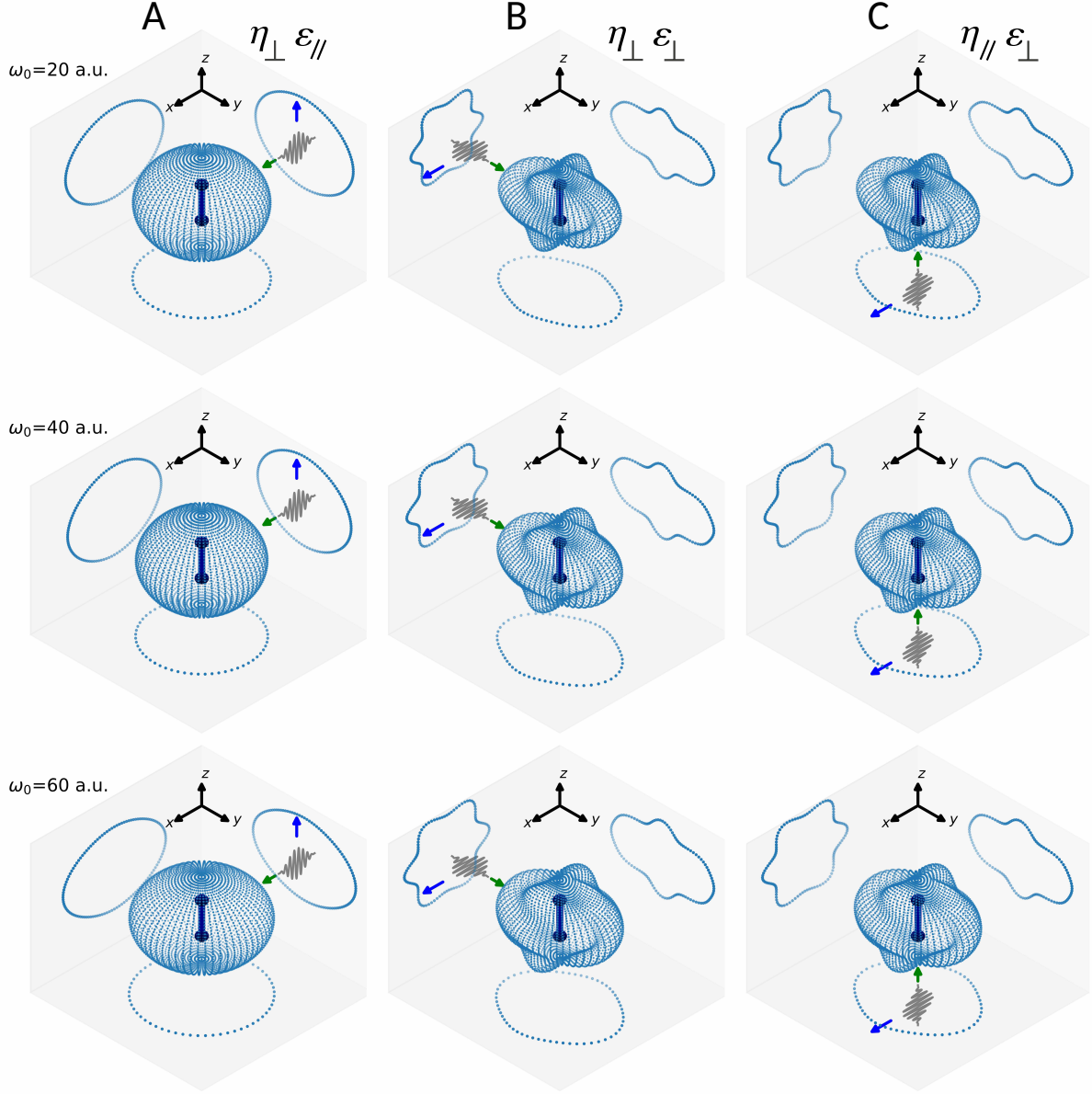


FIG. 5. Same as Fig. 4, but retrieving the MFPADs within the dipole approximation.

the asymmetric electron emission is favored in the backward direction with respect to the propagation direction. Finally, in the C configuration, the asymmetric photoelectron emission with respect to the plane containing the polarization vector and perpendicular to the propagation is found for every pulse because both dipole and nondipole terms significantly contribute to the ionization yields in the SCS region for all central frequencies ω_0 .

Electron emission angular asymmetries have been explored over the years in atoms and molecules as the re-

sult of the coherent superposition of states with different gerade/ungerade symmetries, or equivalently, with scattered electrons carrying even/odd angular momenta. This can be already achieved within a regime where the dipole approximation remains valid by combining light sources with two different colors that induce interferences between processes occurring at different orders. For instance, using an ultrashort UV/XUV pulse and an IR field [49] or employing FEL at two different XUV/soft-X-ray frequencies such that the one-photon absorption of

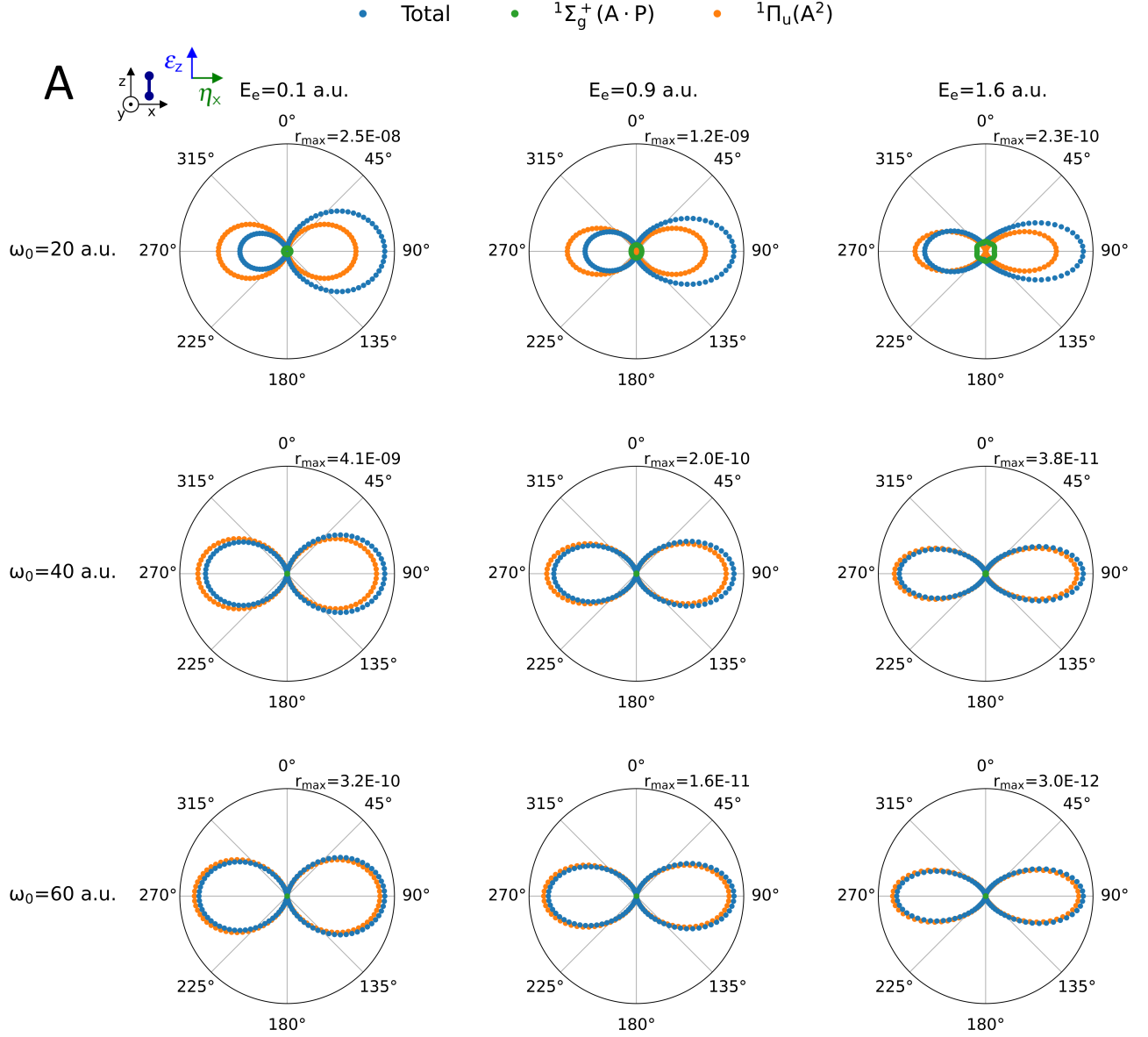


FIG. 6. 2D MFPADs for the A configuration ($\eta_{\perp}\epsilon_{//}$) with the polarization vector along the z -axis and the propagation along x (see inset in the top left of the figure). The 2D projection is performed in the plane defined by the light vectors and positioned at the molecular center of mass. Together with the MFPADs, we show the incoherent contributions associated with the different open channels, i.e. all accessible symmetries through dipole ($^1\Sigma_g^+$) and nondipole transitions ($^1\Pi_u$), are given and indicated in the legend.

ω_1 can reach the same energies as the two-photon absorption of $\omega_2 = \omega_1/2$, but emitting electrons with different angular momenta [50]. In the present SCS process, the different final symmetries are reached at the same (second) order because two different operators ($\mathbf{A} \cdot \mathbf{P}$ or/and \mathbf{A}^2) acting over the ground state of the target are at play on equal footing. Moreover, as we will explain in the following, the molecular orientation provides an extra parameter of control with respect to atoms.

In order to better illustrate the properties of nondipole-induced molecular SCS, we also show the MFPADs that are obtained in a simulation performed within the dipole approximation. Fig. 5 shows these MFPADs for the three pulses and the three configurations, keeping the layout of Figs. 3 and 4. One can see at a glance that the dipole approximation predicts quite distinct distributions. Firstly, for a given configuration, Fig. 5 shows that the shape of the distributions barely varies with the cen-

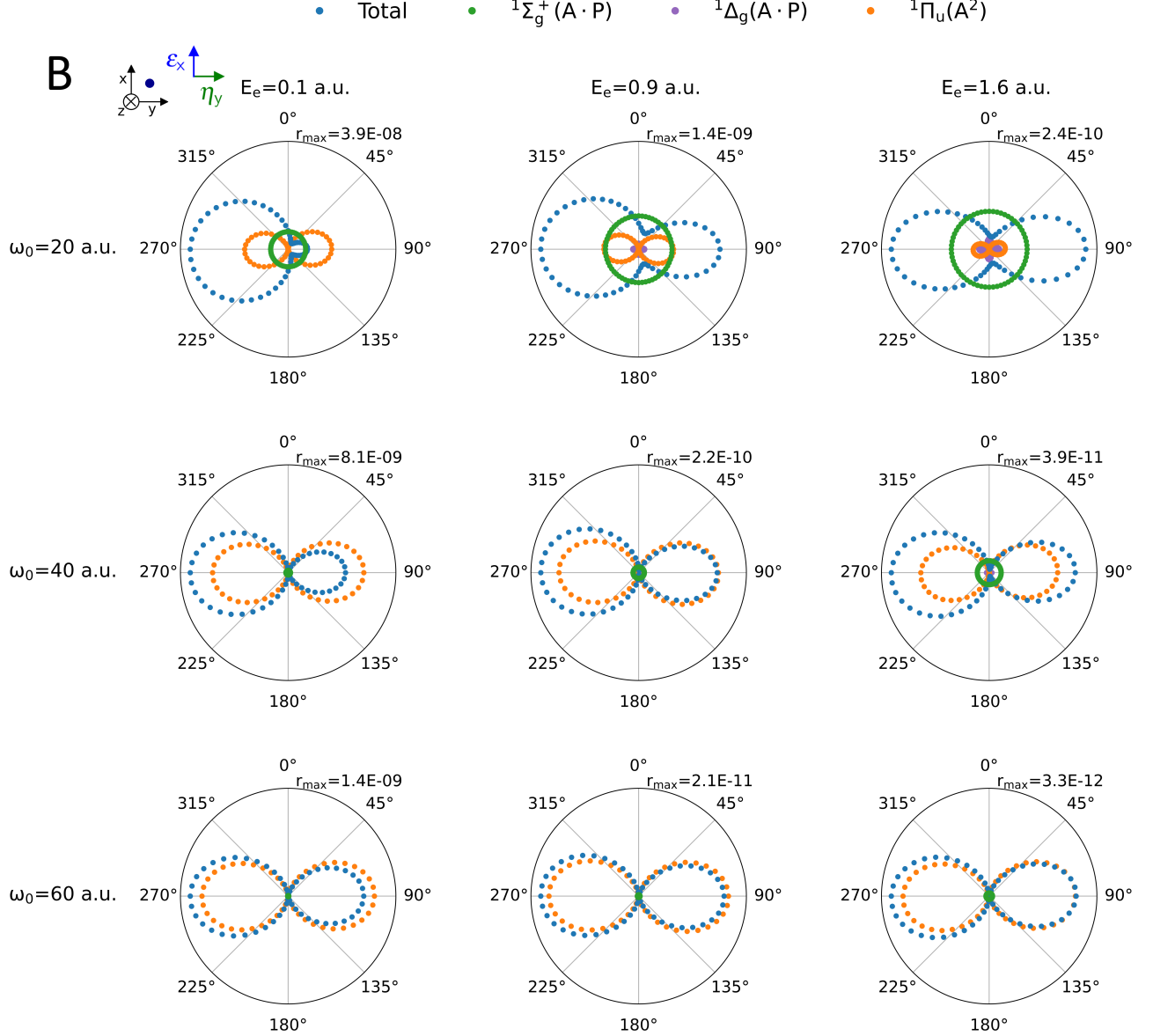


FIG. 7. Same as Fig. 6 for the B configuration, with extra channel $^1\Delta_g$ plotted in purple.

tral frequency ω_0 in dipole approximation. Also, configurations B and C are now equivalent, as already explained. Since the only coupling terms are those involving the dipole operator $(\mathbf{A} \cdot \mathbf{P})$ following ϵ_x (Fig. 2 B and C), the angularly-resolved SCS signal is thus exactly the same for configurations B and C. The complex, but still symmetric, pattern for these angular distributions is due in general to the multicenter character of the molecule. For the A configuration, the dipole-induced MFPADs in the SCS region are quite atomic-like (which favors electron emission with $l = 0$, as already mentioned). For this configuration, the second-order process $^1\Sigma_g^+ \rightarrow ^1\Sigma_u^+ \rightarrow ^1\Sigma_g^+$ (see Eqs. 19) favors the contribution of final electron

emission with $l = 0$ associated with $^1\Sigma_g^+[1s\sigma_g, l = 0]$. This is consistent with the spherical distribution in the electron emission found in the A configuration for every pulse (left column in Fig. 5). For the configurations B and C in the dipole approximation, the predominant channel $^1\Sigma_g^+$ is populated through the second-order process $^1\Sigma_g^+ \rightarrow ^1\Pi_u \rightarrow ^1\Sigma_g^+$. We have found that the largest contribution comes from electrons with $l = 0$, but $l = 2$ has a non-negligible contribution. These two channels contribute resulting in the main features shown in the symmetric MFPADs shown in the middle and right column in Fig. 5. It should be noted that the $^1\Delta_g$ states are also populated (see Fig. 3), and even though the

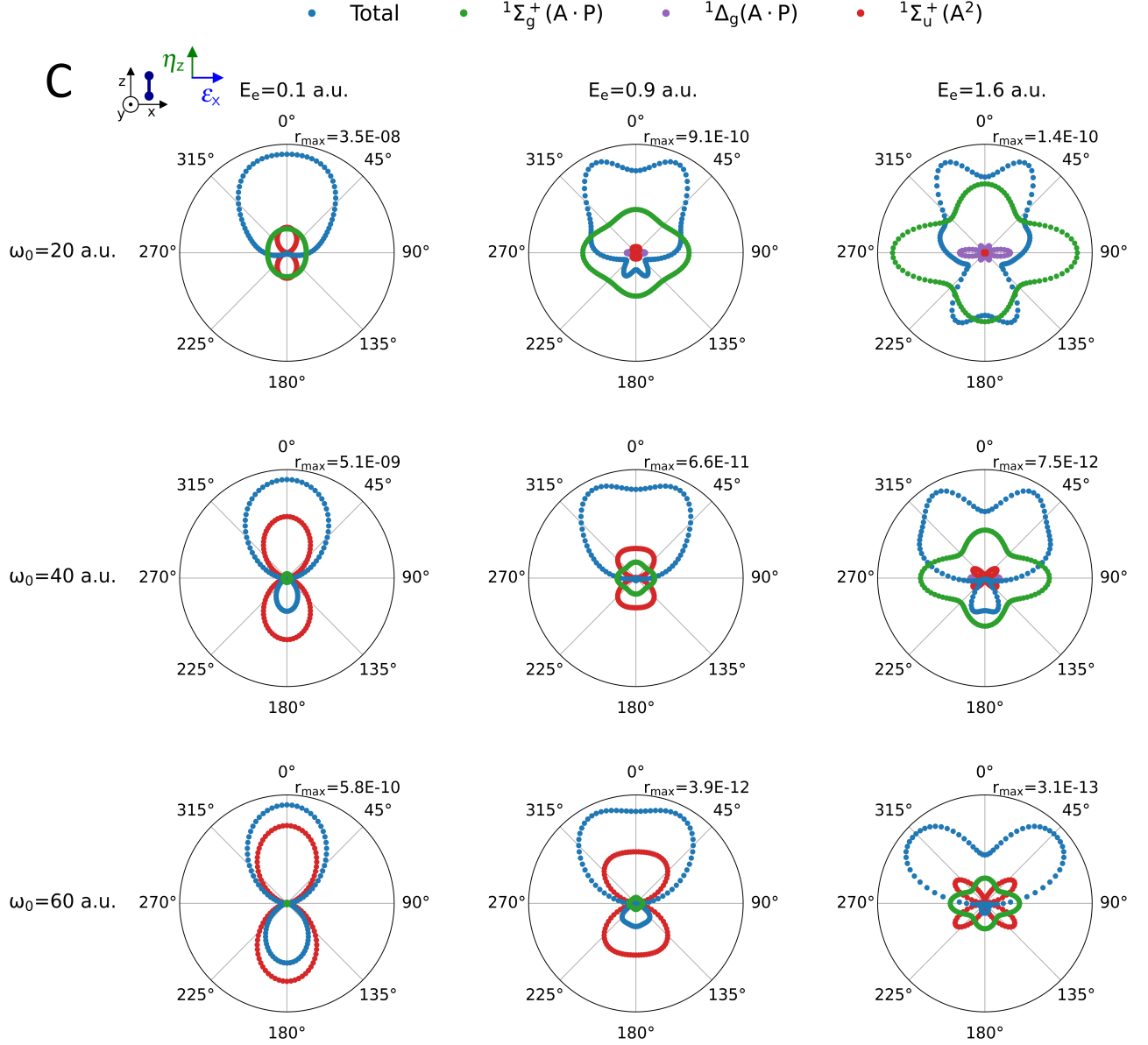


FIG. 8. Same as Fig. 6 for the C configuration.

probability is a couple of orders of magnitude smaller, the resulting MFPADs shown for B and C configurations are also partly shaped by the ${}^1\Delta_g$ contribution. Furthermore, if we compare in Figs. 4 and 5, the cuts in the two planes containing the propagation direction, one perpendicular to the polarization vector and the other parallel, we clearly see that the nearly cylindrical symmetry around the propagation direction η is absent in the dipole approximation. The quite distinct photoelectron distributions of Figs. 4 and 5 thus imply that experimentally it would be possible to disentangle the dipole and nondipole-induced SCS contributions, but also, between the relative contributions of specific symmetries. For a

more detailed analysis of the resulting angular dependencies, we also extract the MFPADs for specific photoelectron energies, including all dipole and nondipole terms. Instead of integrating over the whole electron energy range, we now inspect the angular distributions for three specific photoelectron energies, $E_e = 0.1, 0.9$, and 1.6 a.u., and for completeness in our analysis, we show them for the three pulses ($\omega_0 = 20, 40$, and 60 a.u.) and the three configurations presented in Fig. 2. Fig. 6 shows the angular distributions for the three pulses and the three photoelectron energies for the light-molecule configuration A ($\eta_{\perp}\varepsilon_{//}$). Fig. 7 shows the same results for a B configuration ($\eta_{\perp}\varepsilon_{\perp}$) and Fig. 8 for C ($\eta_{//}\varepsilon_{\perp}$).

We now include not only the resulting angular distribution but also the incoherent contribution of each accessible final symmetry. To better visualize each contribution, instead of a three-dimensional plot, we now plot only a cut of the angular distribution containing the symmetry plane given by the light, i.e. the plane defined by the polarization and the propagation vector: for the A configuration in Fig. 6, we present a cut in the xz plane, for the B configuration in Fig. 7 in xy , and for the C configuration in Fig. 8 in xz .

As we have seen in the left column of Fig. 3, for the A configuration, nondipole-induced SCS dominates at any photoelectron energy for the three pulses, with a larger predominance for large ω_0 and for low electron energy. As a result, we can see in Fig. 6 an almost symmetric electron emission for central frequencies of 40 and 60 a.u. We see the reflection symmetry relative to the zy plane associated with the \mathbf{A}^2 term, since, to first-order in $1/c$ this term reduces to $A(t)F(t)\sum_{i=1,2} x_i/c$ (see Eq. 4), leading to a forward/backward asymmetry of the electron emission along the x -axis. This symmetry is broken in the total MFPAD (blue dots). As expected, as the dipole term becomes larger for 20 a.u. photon energy, the electron asymmetry clearly manifests, being more pronounced for the lowest electron energy (0.1 a.u.). An interesting feature shown in Fig. 6 is the trend found as the electron energy increases, where the MFPAD becomes more directional towards the propagation vector η_x .

In Fig. 7, we show the corresponding MFPADs for the B configuration. Now, for every photon and electron energy, the asymmetric electron emission is appreciable, being larger at 20 a.u. photon energy and lower electron energies, where dipole and nondipole terms are comparable in magnitude. We also clearly see that the electron emission is in the backward direction with respect to the propagation direction, a feature already noticed in the discussion of Fig. 4, which is more pronounced when the nondipole contribution is of the order of magnitude of the dipole one.

For the C configuration, in Fig. 8, one finds the strongest variation in the MFPADs with pulse and electron energies, as was expected from the remarkable competition between channels shown in Fig. 3. We focus on the 20 a.u. pulse, i.e. first row in Fig. 8. For the electron energy 0.1 a.u. closest to threshold, the largest asymmetry is found as a result of the coherent superposition of the $^1\Sigma_g^+$ (green dots) and $^1\Sigma_u^+$ (red dots) states populated through the dipole $\mathbf{A} \cdot \mathbf{P}$ and nondipole \mathbf{A}^2 terms, respectively. In this case, a pure dipole transition would lead to almost spherical emission associated with $^1\Sigma_g^+$, where the H_2^+ is left behind in its $X^2\Sigma_g^+(1s\sigma_g)$ ground state and the electron is emitted as a combination of even angular momenta, mostly $l = 0$ as revealed in the distribution in green dots. The $^1\Sigma_u^+$ symmetry (red dots) reached through the nondipole terms leads to an electron emission mostly given by an $l = 1$ angular momentum. Because these two amplitudes now present similar mag-

nitude, one finds a highly asymmetric electron emission. For larger electron energies, 0.9 and 1.6 a.u., we observe that a pure dipole transition into the $^1\Sigma_g^+$ (green dots) already produces the complex but still symmetric pattern previously mentioned, because a higher angular momentum ($l = 2$) is also contributing. Moreover, we see an increased probability associated with the dipole transition into the $^1\Delta_g$ states (purple dots). Even though the dipole-driven amplitudes are significantly smaller than the nondipole-induced ones, the coherent sum leads to a noticeable asymmetry as seen in the bottom row left of Fig. 8. We now focus on the left column of Fig. 8 to examine the variation of the MFPADs for a given electron energy as we increase the central photon energies ω_0 . As the photon energy increases, the nondipole term (\mathbf{A}^2 in red dots) also increases, reaching values orders of magnitude larger than the dipole counterpart, leading to a less pronounced asymmetry. As illustrated in Fig. 8, the largest asymmetries are found when the relative amplitudes reach similar values in specific electron emission directions, i.e. for the 20 a.u. pulse with the lowest electron energies (e.g., 0.1 a.u., first row left column in Fig. 8), or for the 60 a.u. pulse for the largest electron energies (e.g., 1.6 a.u., bottom row right column in Fig. 8).

IV. CONCLUSIONS

We have theoretically investigated close-to-threshold ionization of H_2 by stimulated Compton scattering using an ultrashort soft X-ray pulse. As a proof of concept, we provide simulations within a nonperturbative nonrelativistic approximation with frozen nuclei at the equilibrium distance. Stimulated Compton scattering can be induced by using soft and X-ray pulses as those currently generated in free-electron laser facilities. The present schemes could be achieved with a single pulse having a duration of few tens of attoseconds or, alternatively, with two collinear soft X-ray pulses of different colors. We have simulated the angularly and energy-resolved photoionization yields that would result after the interaction of H_2 with three different pulses of 66 attoseconds duration and 10^{18} W/cm^2 , centered around photon energies of 20, 40, and 60 a.u., respectively. We have checked that, under these conditions, the perturbative regime holds and therefore the SCS rates vary quadratically with the intensity. The large energy bandwidth of the pulse allows for the absorption and subsequent emission of photons leading to ionization close to threshold. We have shown that with these laser parameters molecular SCS proceeds through both dipole and nondipole induced transitions. As a consequence, the coherent emission of electrons through different quantum paths leads to controllable asymmetric electron emission. We have shown that molecular SCS provides three knobs of control: (i) the molecular axis, (ii) the light polarization, and (iii) the light propagation direction, thus offering a much

richer scenario than the atomic SCS. We hope that the present study will stimulate experimental investigations of molecular SCS by combining sub-fs XFEL pulses with multicoincidence detection techniques.

ACKNOWLEDGMENTS

Work supported by the European COST Action AttoChem CA18222, the French National Research Agency (ANR) in the frame of "the Investments for the future"

Programme IdEx Bordeaux - LAPHIA (ANR-10-IDEX-03-02), and the Spanish Ministry of Science and Innovation MICINN through the projects PDI2019-105458RB-I00, the "Severo Ochoa" Programme for Centres of Excellence in R&D (SEV-2016-0686) and the "María de Maeztu" Programme for Units of Excellence in R&D (CEX2018-000805-M). The authors thank the University of Bordeaux for providing access to the Mésocentre de Calcul Intensif Aquitaine (MCIA), the MareNostrum in the Barcelona Supercomputing Center through the Spanish Supercomputing Network and in the Centro Computación Científica at UAM.

-
- [1] W. Ackermann *et al*, Nat. Photonics **1**, 336 (2007).
 - [2] P. Emma *et al*, Nat. Photonics **4**, 641 (2010).
 - [3] S. Jamison, Nat. Photonics **4**, 589 (2010).
 - [4] T. Ishikawa *et al*, Nat. Photonics **6**, 540 (2012).
 - [5] M. Allaria *et al*, Nat. Photonics **6**, 699 (2012).
 - [6] H.-S. Kang *et al*, Nat. Photonics **11**, 708 (2017).
 - [7] T. Tschentscher, C. Bressler, J. Grünert, A. Madsen, A.P. Mancuso, M. Meyer, A. Scherz, H. Sinn, and U. Zastrau, Appl. Sci. **7**, 592 (2017).
 - [8] C.J. Milne *et al*, Appl. Sci. **7**, 720 (2017).
 - [9] C. Bostedt *et al*, Rev. Mod. Phys. **88**, 015007 (2016).
 - [10] E.A. Seddon *et al*, Rep. Prog. Phys. **80**, 115901 (2017).
 - [11] L. Young *et al*, J. Phys. B **51**, 032003 (2018).
 - [12] E. Hemsing, G. Stupakov, D. Xiang, and A. Zholent, Rev. Mod. Phys. **86**, 897 (2014).
 - [13] S. Huang, Y. Ding, Y. Feng, E. Hemsing, Z. Huang, J. Krzywinski, A. A. Lutman, A. Marinelli, T. J. Maxwell, and D. Zhu, Phys. Rev. Lett. **119**, 154801 (2017).
 - [14] M. Hentschel, R. Kienberger, C. Spielmann, G.A. Reider, N. Milosevic, T. Brabec, P. Corkum, U. Heinzmann, M. Drescher, and F. Krausz, Nature **414**, 509 (2001).
 - [15] T. Gaumnitz, A. Jain, Y. Pertot, M. Huppert, I. Jordan, F. Ardana-Lamas, and H. J. Wörner, Optics Express **25**, 27506 (2017).
 - [16] R. Bartels, S. Backus, I. Christov, H. Kapteyn, and M. Murnane, Chemical Physics **267**, 277 (2001).
 - [17] M.-C. Chen *et al*, Proceedings of the National Academy of Sciences **111**, E2361 (2014).
 - [18] N. Hartmann *et al*, Nat. Photonics **12**, 215 (2018).
 - [19] J. Duris *et al*, Nat. Photonics **14**, 30 (2020).
 - [20] H. Fukuzawa *et al*, Nat. Comm. **10**, 2186 (2019).
 - [21] S. Li, T. Driver, O. Alexander, B. Cooper, D. Garratt, A. Marinelli, J. P. Cryan, and J. P. Marangos, Faraday Discussions (2021), 10.1039/D0FD00122H.
 - [22] A.A. Lutman, R. Coffee, Y. Ding, Z. Huang, J. Krzywinski, T. Maxwell, M. Messerschmidt, and H.-D. Nuhn, Phys. Rev. Lett. **110**, 134801 (2013).
 - [23] G. De Ninno, B. Mahieu, E. Allaria, L. Giannessi, and S. Spampinati, Phys. Rev. Lett. **110**, 064801 (2013).
 - [24] T. Hara *et al*, Nat. Commun. **4**, 2919 (2013).
 - [25] S. Serkez *et al*, App. Phys. **10**, 2728 (2020).
 - [26] Doumy G. *et al*, Phys. Rev. Lett. **106**, 083002 (2011).
 - [27] M. Fuchs, Nat. Phys. **11**, 964 (2015).
 - [28] H. Dörner, V. Mergel, O. Jagutzki, L. Spielberger, J. Ullrich, R. Moshhammer, and H. Schmidt-Böcking, Phys. Rep. **330**, 95 (2000).
 - [29] M. Kircher *et al*, Nat. Phys. **16**, 756 (2020).
 - [30] S. Grundmann *et al*, Science **370**, 339 (2020).
 - [31] H. Bachau and M. Dondera, Europhys. Lett. **114**, 23001 (2016).
 - [32] M. Dondera, V. Florescu, and H. Bachau, Phys. Rev. A **95**, 023417 (2017).
 - [33] H. Bachau, M. Dondera, and V. Florescu, Phys. Rev. Lett. **112**, 073001 (2014).
 - [34] M. Dondera, V. Florescu, and H. Bachau, Phys. Rev. A **90**, 033423 (2014).
 - [35] M. Dondera and H. Bachau, Phys. Rev. A **85**, 013423 (2012).
 - [36] A. Sopena, A. Palacios, F. Catoire, H. Bachau, and F. Martín, Commun. Phys., *in press* (2021).
 - [37] H. Bachau, E. Cormier, P. Decleva, J.E. Hansen, and F. Martín, Rep. Prog. Phys. **64**, 1815 (2001).
 - [38] F. Martín, J. Phys. B **32**, R197 (1999).
 - [39] A. Palacios, J.L. Sanz-Vicario, and F. Martín, J. Phys. B **48**, 242001 (2015).
 - [40] A. Palacios, S. Barmaki, H. Bachau, and F. Martín, Phys. Rev. A **71**, 063405 (2005).
 - [41] R. Anzaki, Y. Shinohara, T. Sato, and K. L. Ishikawa, Phys. Rev. A **98**, 063410 (2018).
 - [42] A. D. Bandrauk, F. Fillion-Gourdeau, and E. Lorin, J. Phys. B **46**, 153001 (2013).
 - [43] H. A. Kramers and W. Heisenberg, Z. Phys. **31**, 681 (1925).
 - [44] I. Waller, Z. Phys. **51**, 213 (1928).
 - [45] M. Gavrila, Phys. Rev. A **6**, 1348 (1972).
 - [46] L.V. Keldysh, Sov. Phys. JETP **20**, 1307 (1965).
 - [47] P. Eisenberger and P. M. Platzman, Physical Review A **2**, 415 (1970).
 - [48] O.A. Fojón, J. Fernández, A. Palacios, R.D. Rivarola, and F. Martín, J. Phys. B **37**, 3035 (2004).
 - [49] R. Y. Bello, F. Martín, and A. Palacios, Faraday Discussions (2021), 10.1039/D0FD00114G.
 - [50] K.C. Prince *et al*, Nat. Photonics **10**, 176 (2016).